Humidity-Modulated Phase Control and Nanoscopic Transport in Supramolecular Assemblies

Ying Chen,[†,‡] Mark D. Lingwood,[†,§,‡] Mithun Goswami,[†] Bryce E. Kidd,[†] Jaime J. Hernandez,[⊥] Martin Rosenthal,[∥] Dimitri A. Ivanov,[⊥,∥,*] Jan Perlich,[○] Heng Zhang,[#] Xiaomin Zhu,[#] Martin Möller,[#] and Louis A. Madsen[†,*]

[†]Department of Chemistry and Macromolecules and Interfaces Institute, Virginia Polytechnic Institute and State University, Blacksburg, Virginia, 24061, United States

[§]Department of Chemistry, Saint Mary's College of California, 1928 Saint Mary's Road, Moraga, California, 94556, United States

[⊥]Institut de Sciences des Matériaux de Mulhouse (IS2M-CNRS), CNRS UMR 7361, 15 rue Jean Starcky, Mulhouse, 68057, France

[∥]Faculty of Fundamental Physical and Chemical Engineering, Moscow State University. GSP-1, Leninskie Gory, 119991, Moscow, Russia

[○]DESY-HASYLAB, Notkestrasse 85, 22607 Hamburg, Germany

[#]Interactive Materials Research−DWI an der RWTH Aachen e.V. and Institute of Technical and Macromolecular Chemistry, RWTH Aachen University, Forckenbeckstrasse 50, 52056 Aachen, Germany

S *Supporting Information*

ABSTRACT: Supramolecular assembly allows for enhanced control of bulk material properties through the fine modulation of intermolecular interactions. We present a comprehensive study of a cross-linkable amphiphilic wedge molecule based on a sulfonated trialkoxybenzene with a sodium counterion that forms liquid crystalline (LC) phases with ionic nanochannel structures. This compound exhibits drastic structural changes as a function of relative humidity (RH). Our combined structural, dynamical, and transport studies reveal deep and novel information on the coupling of water and wedge molecule transport to structural motifs, including the significant influence of domain boundaries within the material. Over a range of RH values, we employ ^{23}Na solid-state NMR on the counterions to complement detailed structural studies by grazing-incidence small-angle X-ray scattering. RH-dependent pulsed-field-gradient (PFG) NMR diffusion studies on both water and the wedge amphiphiles show

Increased Relative Humidity

multiple components, corresponding to species diffusing within LC domains as well as in the domain boundaries that compose 10% of the material. The rich transport and dynamical behaviors described here represent an important window into the world of supramolecular soft materials, carrying implications for optimization of these materials in many venues. Cubic phases present at high RH show fast transport of water (2×10^{-10} m^2/s), competitive with that observed in benchmark polymeric ion conductors. Understanding the self-assembly of these supramolecular building blocks shows promise for generating cross-linked membranes with fast ion conduction for applications such as next-generation batteries.
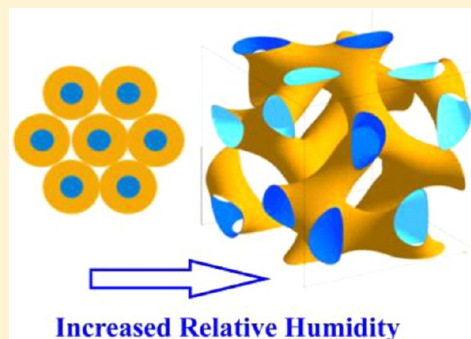
INTRODUCTION

Supramolecular assemblies can arise from molecular building blocks with specifically designed intermolecular interactions, such as hydrogen bonding, ionic interactions, ion-dipolar interactions, π-stacking as well as excluded volume repulsion and shape anisotropy.[1−4] Such assemblies allow for increased degrees of freedom in controlling macroscopic material properties, and currently we are targeting fast ion conduction for batteries, solar cells, and fuel cells. In particular, supra-molecular materials show promise for fine control of morphology on many length scales, including the local (few nm) length scale that principally governs ion motion.[5−8] Many studies have explored liquid crystalline (LC) structures formed from supramolecular assemblies for ion conduction applica-

tions,[9−14] however the multimodal characterization of such materials to correlate transport information and structure at the molecular level has been limited. Here we describe a set of subtle mesophase manipulations coupled with sensitive and correlated measurements of structure and transport on a polymerizable wedge-shaped sulfonate amphiphile. These results represent a new pathway to material control in supramolecular phases composed of amphiphilic molecular building blocks.
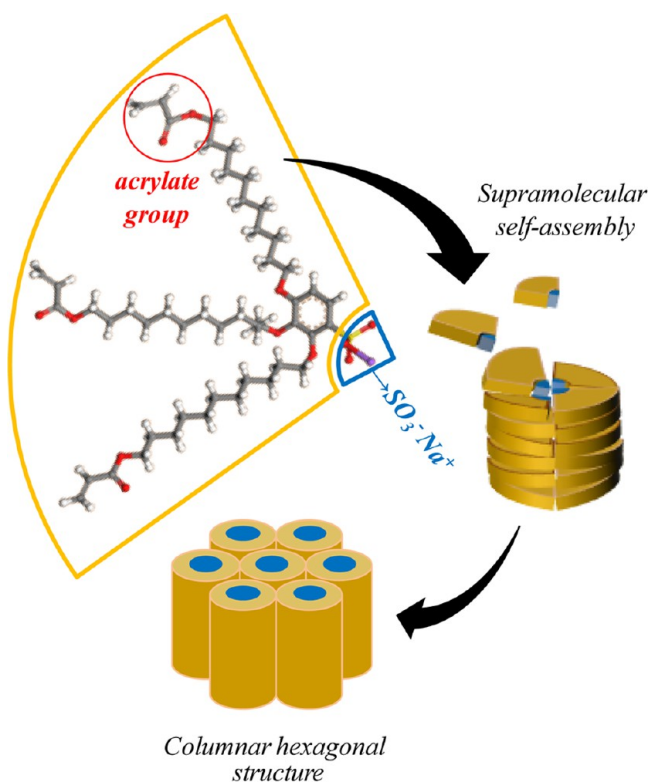
Figure 1. Molecular structure of the acrylate sulfonate wedge molecules used in this work. Self-assembly of the mesogen begins with formation of supramolecular disks (tetramers) and continues toward the classical 2D hexagonal columnar structure (at lower humidity values) with ion conducting channels running along the column axes. When exposed to high humidity, this structure readily transforms to bicontinuous cubic structures characterized by fast water transport.[15]

Figure 1 shows the amphiphile molecular structure as well as a representative supramolecular self-assembly process to form columnar phases. In these novel systems, exposure to humid air drastically alters self-assembly, allowing for sensitive control of phase, as shown in our previous work.[15] Using these manipulations, we can define nanostructures with optimal geometry, dimensions, and dynamics for ion transport.

To correlate material structure with ion transport and to understand the mechanisms of ion conduction, it is crucial to combine multiple techniques that probe the structure and dynamics of soft materials. In this paper, we probe supra-molecular structure in detail using *in situ* synchrotron grazing-incidence small-angle X-ray scattering (GISAXS) as a function of relative humidity (RH). We also showcase the use of ^{23}Na solid-state NMR (SSNMR) to reveal drastic RH-dependent structural and ion association changes in these amphiphilic sodium salts. Further, we investigate the transport dynamics using pulsed-field-gradient (PFG) NMR diffusometry, showing that water transport in these materials depends intimately on supramolecular structure. The unique combination of NMR spectroscopy and diffusometry with high resolution X-ray scattering provides new insights into the coupling of structure and morphology with molecular transport.

EXPERIMENTAL SECTION

Acrylated Wedge Molecule Synthesis and Film Preparation. We define the amphiphilic wedge molecules as "**A-Na**" (for acrylated molecule, sodium salt) as shown in Scheme 1. Synthesis details were described in our previous

Scheme 1. Chemical Structure of Sodium 2,3,4-Tris(11′-acryloyloxyundecyl-1′-oxy)benzenesulfonate (A-Na)
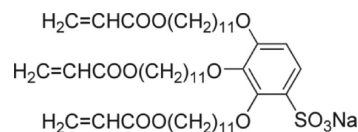
work.[15] **A-Na** thin films used in X-ray studies were prepared by spin-coating from solutions in CHCl$_3$ (20 mg · ml^{-1}) over Si substrates. Prior to film deposition, substrates were cleaned by immersion in piranha solution (H$_2$SO$_4$:H$_2$O$_2$, 3:1) and abundant rinsing with deionized water. **A-Na** salt was used in its pure bulk form as received (a waxy solid) for all NMR studies.

X-ray Scattering Studies. Characterization of the **A-Na** films was carried out by grazing-incidence small-angle X-ray scattering (GISAXS), a powerful technique in structural investigations of thin organic films.[16,17] GISAXS measurements were performed at the BW4 beamline of HASYLAB (Hamburg, Germany); the wavelength used was λ = 1.38 Å. X-ray patterns were recorded at room temperature using a 2D CCD camera. The norm of the scattering vector **s** ($|s| = (2 \sin\theta)/\lambda$, where θ is the Bragg angle) was calibrated using a silver behenate standard. Samples were precisely aligned to an angle of 0.4° with respect to the incident beam. This relatively high value allowed avoidance of the Bragg peaks due to the reflected beam, which is a frequent observation in the GISAXS configuration.[18] Immediately prior to GISAXS measurements, samples were equilibrated at a range of RH-values for at least 1.5 h, generated by saturated solutions of inorganic salts in D$_2$O (see Table 1).

Table 1. Inorganic Salts Used in the GISAXS and NMR Experiments and RH Conditions Obtained above Their Saturated Solutions with D$_2$O

salt	RH (%)
MgCl$_2$	33
Mg(NO$_3$)$_2$	55
KCl	86
pure D$_2$O	100

These various salt solutions create a well-defined RH atmosphere above them due to the different activity of water for the salt solutions.[19] The humidity level was measured using a digital humidity sensor (Sensirion SHT75). The sample is equilibrated above these solutions for controllable and reproducible water uptake. Water uptake, expressed in $\lambda(H_2O/SO_3^-)$, was determined using the following equation:

$$\lambda(H_2O/SO_3^-) = \frac{\text{mass}_{\text{wet}} - \text{mass}_{\text{dry}}}{\text{mass}_{\text{dry}}} \times \frac{MW_{\text{A-Na}}}{MW_{H_2O}}$$

Here mass$_{\text{dry}}$ stands for the mass of vacuum-dried **A-Na** material, mass$_{\text{wet}}$ is the mass of wet **A-Na** equilibrated above various salt solutions, while $MW_{\text{A-Na}}$ and MW_{H_2O} are molecular weight of **A-Na** and water, respectively. To this end, **A-Na** films were placed in a sealed environmental chamber as depicted in Figure 2.
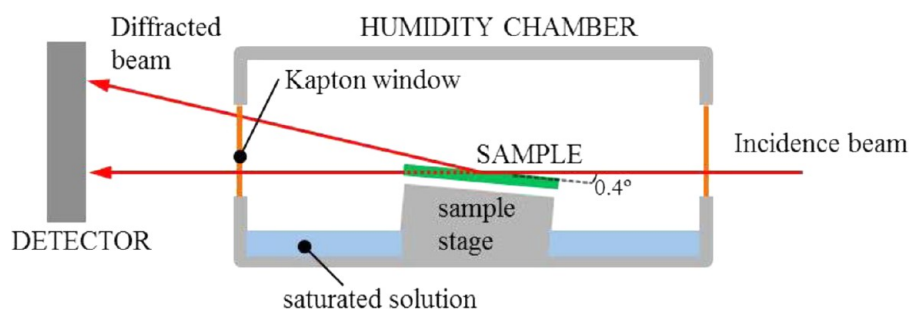
Figure 2. Schematic of synchrotron GISAXS setup. The custom-built chamber allows equilibration above humid atmosphere at controlled RH.
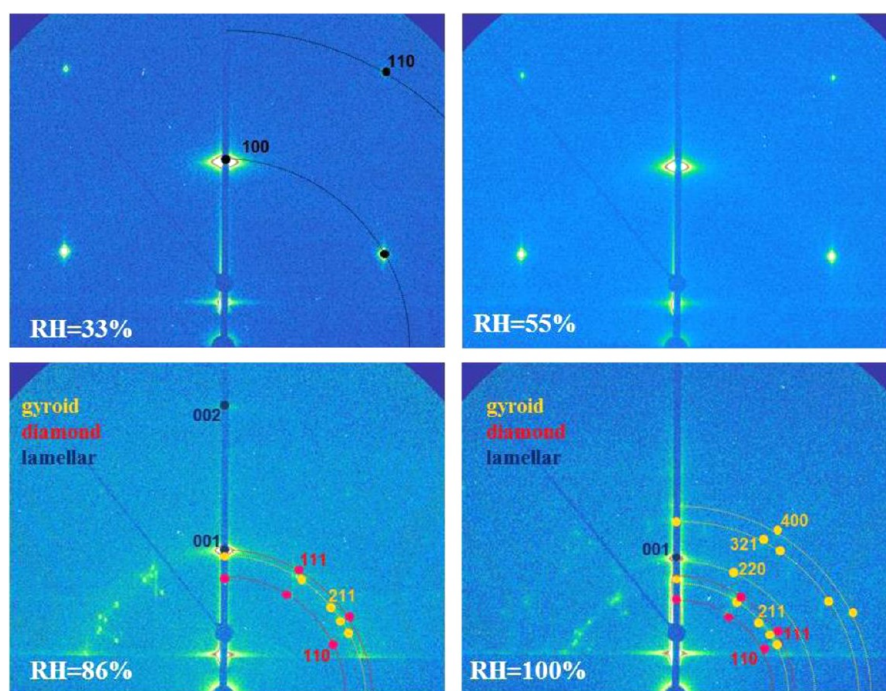

Figure 3. 2D X-ray patterns vs RH. At RH ≤ 55%, only the hexagonal columnar phase exists, while at RH ≥ 86% we observe predominantly bicontinuous cubic gyroid and diamond phases together with a lamellar phase. We highlight the main peaks of each phase (see also Table 2).

NMR Studies. All solid-state NMR experiments were performed on a Bruker Avance III 600 MHz (14.1 T) spectrometer using a 3.2 mm HXY probe. **A-Na** salt was packed into a 3.2 mm magic angle spinning (MAS) zirconia rotor, which was then exposed to various hydration levels by placing the rotor over different solutions for ≥1 day (Table 1) in sealed chambers. Before measurement, the rotor was removed from the hydration chamber and quickly capped. Experiments were performed at 10 kHz and 18 kHz spinning speeds at the magic angle (54.74°). No spinning side bands were observed for ^{23}Na MAS spectra with a spinning speed of 10 kHz. NMR spectra under static conditions were also recorded. Solid NaCl was used as external reference for ^{23}Na, and solid tetrakis(trimethylsilyl)silane was used as an external reference for ^{1}H.[20−22] To achieve uniform excitation, a short single pulse with 2 μs duration corresponding to 30° tilt angle was used. A total of 1024 and 8 transients with a relaxation delay of 5 s were recorded for ^{23}Na and ^{1}H spectra, respectively. All experiments were conducted at 25 °C.

For relaxation and diffusion measurements, bulk solid **A-Na** was divided into five samples of 10−20 mg each. Each sample was placed into a 1 cm length of 4 mm glass tubing (2 mm inner diameter) with one end sealed, and placed on a vacuum

line at 1 mTorr for 2 days. Following evacuation, one sample was transferred into a 5 mm NMR tube and sealed under vacuum. The remaining four samples were held above various solutions (Table 1) at room temperature for ≥1 day. Immediately prior to NMR measurements, samples were removed from RH-equilibration tubes and placed into 5 mm NMR tubes along with a length of 4 mm glass rod (to reduce dead volume) and capped.

All PFG NMR diffusion measurements were obtained using a Bruker Avance III wide bore 400 MHz (9.4 T) NMR equipped with a Diff60 diffusion probe and either a 5 mm ^{1}H or 5 mm ^{2}H/^{1}H coil (Bruker Biospin, Billerica, MA). The pulsed-gradient stimulated echo (PGSTE) sequence[23] was used to measure diffusion, with an effective gradient pulse length of δ = 2 ms (the actual pulse length of the sinusoidal pulse was 3.15 ms), a 2 ms gradient stabilization time after each gradient pulse, a gradient pulse spacing of Δ = 50 ms, and gradient strengths varying from g = 20 G/cm to g = 1800 G/cm. Sixteen to 32 gradient steps were applied, and the number of scans varied from 4 to 64 to yield sufficient signal-to-noise ratio (SNR). Diffusion was measured along the magnetic field (z) direction. The self-diffusion coefficient D was obtained by fitting the

measured signal intensity I as a function of gradient strength g to the Stejskal−Tanner equation:[23,24]

$$I = I_0 e^{-D\gamma^2 g^2 \delta^2 (\Delta - \delta/3)} = I_0 e^{-Db} \tag{1}$$

where γ is the gyromagnetic ratio of the detected nucleus, and the Stejskal−Tanner factor $b = \gamma^2 g^2 \delta^2 (\Delta - \delta/3)$. All PFG NMR experiments were conducted at 25 °C. The spin−lattice relaxation time T_1 was measured by the inversion−recovery method. The spin−spin relaxation time T_2 was measured using an incremented echo-train CPMG pulse sequence. Errors in T_1 and T_2 values are ±3%, and errors in D are ±5%.

■ RESULTS AND DISCUSSION

Through our coordinated GISAXS and NMR measurements, we present a detailed picture of the supramolecular structure in the **A-Na** material and how mesophase structure, channel dimensions, amorphous character, and domain boundaries influence molecular transport.

X-ray Scattering. We show X-ray diffractograms as a function of relative humidity (RH) in Figure 3, with Miller indices of the main reflections indicated in each case. Since the patterns are symmetric, we use only one quadrant (Figure 3) for peak assignment. The GISAXS patterns show highly oriented film textures. At RH = 33 and 55%, we observe peaks with a ratio of d-spacings of $1:1/\sqrt{3}$. Using the angular positions and d-spacings of the peaks, we assign these peaks to the 100 and 110 reflections of a hexagonal columnar disordered mesophase (Col_{hd}). Importantly, the film exhibits planar orientation, i.e., the column axes lie in the substrate plane. Water absorption of **A-Na** at RH = 55% results in an increase of the lattice parameter from 39.2 to 40.3 Å, i.e., by 3%. At higher RH the mesophase undergoes a phase transition, as inferred from changes in X-ray patterns observed at RH = 86% and 100%. Using the d-spacing ratios ($\sqrt{6}:\sqrt{8}:\sqrt{14}:\sqrt{16}$ and $\sqrt{2}:\sqrt{3}$) and the angular positions of the new peaks, we identify two cubic bicontinuous phases (Cub_{bi}), specifically the gyroid (G) and diamond (D) phases. These conclusions are qualitatively similar to those drawn in our previous work,[15] where the phase behavior of thin films of **A-Na** was studied in nonequilibrium conditions in H_2O-saturated atmosphere. However, it is noteworthy that in the present work the phase structure is addressed in quasi-equilibrium conditions using D_2O vapors to match the conditions of NMR experiments. This difference likely accounts for the fact that, in addition to the two bicontinuous cubic phases observed previously, we see an additional pair of peaks with a d-spacing ratio of 1:2, which we assign to a lamellar phase. Table 2 summarizes the hkl-indices of the observed peaks and lattice parameters. Importantly, the new phases grow epitaxially on the parent Col_{hd}, similar to previous reports.[25−27]

Generally, the diamond and gyroid phases are related by the so-called Bonnet transformation. The Bonnet symmetry implies that the energy of the minimal surfaces of the two structures is degenerate. For this symmetry, the relation between lattice parameters of the unit cells should be $a_G/a_D = 1.57$.[20] In our case, at RH ≥ 86%, we found this ratio to be constant and equal to 1.49. This difference might be explained by distortions during the G-D transition[28] or as a consequence of confinement imposed by the thin film.

The Cub_{bi} phases appear in the phase diagram of amphiphiles during lyotropic transitions, and are located between the columnar and lamellar structures.[29] The observed

Table 2. Diffraction Peaks Pertinent to the Different Phases Formed at Different RH Values and the Corresponding Lattice Parameters

RH (%)	phase	hkl	d_{exp} [nm]	d_{calc} [nm]	lattice parameters [nm]
33	Col_{hd}	100	3.40	3.39	$a = 3.92$
		110	1.97	1.97	
55	Col_{hd}	100	3.49	3.49	$a = 4.03$
		110	2.03	2.02	
86	Cub_{bi}(G)	211	4.49	4.49	$a = 11.01$
	Cub_{bi}(D)	110	5.22	5.25	$a = 7.43$
		200	4.32	4.29	
	lamellar	001	4.31	4.33	4.33
		002	2.18	2.16	
100	Cub_{bi}(G)	211	5.54	5.53	$a = 13.54$
		220	4.62	4.72	
		321	3.58	3.62	
		400	3.32	3.36	
	Cub_{bi}(D)	110	6.44	6.47	$a = 9.16$
		111	5.32	5.29	
	lamellar	001	4.61	4.61	4.61

coexistence of the G, D, and lamellar phases may be thought of as a violation of the classical Gibbs phase rule. One of the reasons for such apparent violation can be the metastable behavior of the phases in this composition range.[30] Indeed, it is noteworthy that the free energy differences between the cub_{bi} phases can be quite subtle. They are typically introduced into models only in a rather detailed treatment of chain stretching contributions, thermal fluctuations or of van der Waals or electrostatic interactions.[31] Therefore, even a slightly metastable character of the system can bring about phase coexistence. In our case, observation of the usual epitaxial relations such as the equivalence of the 10_{hd} and 211_G peaks means that the phase transitions in **A-Na** operate according to the previously reported mechanisms.[25] However, contrary to the situation described in ref 25, the films of **A-Na** do not form well-defined optical textures. It is thus possible that the phase transformation process stays incomplete due to pinning of the growing domains at the grain boundaries. Previously, the difficulty to reach equilibrium conditions was mentioned for studies of the phase diagrams of amphiphiles.[30] In particular, the metastable behavior of the cubic phases caused transformation rates significantly longer than the typical experiment duration.

Figure 4 presents the evolution of lattice parameters as a function of RH at room temperature. The columnar phase (Col_{hd}) swells only to a modest degree (3% in linear dimension) when going from RH = 33% to RH = 55%, while increased water uptake induces stronger swelling of the Cub_{bi} structures between 86% and 100% RH (up to 20% swelling). The lamellar structure swells approximately 6% from 86% to 100% RH.

The diamond and gyroidal phases are two of the three known stable bicontinuous cubic phases (primitive cubic being the third).[32] These Cub_{bi} phases contain one single amphiphilic bilayer, which forms a triply periodic minimal surface (TPMS) with cubic symmetry, giving rise to a 3D continuous ion channel network as depicted in Figure 4 and drawn to scale in Figure 5. By analyzing the lattice parameters and **A-Na** molecular sizes, we estimate the ion channel dimensions. As detailed in the accompanying electronic Supporting Informa-
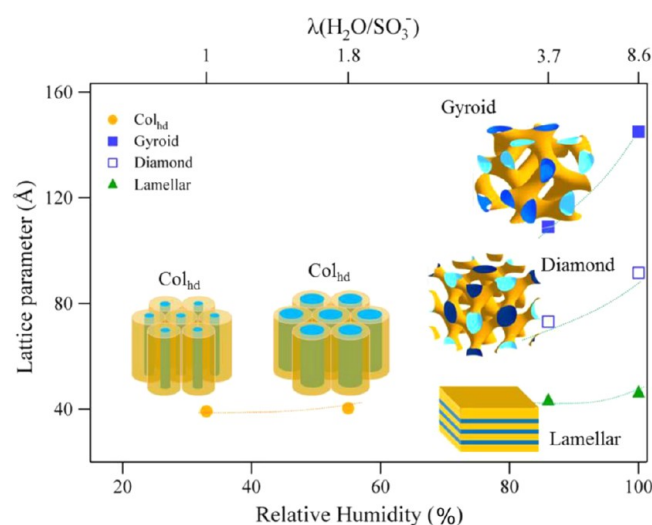
Figure 4. Evolution of the lattice parameter as a function of RH (bottom horizontal axis) and water uptake (top horizontal axis) for **A-Na** in different mesophases. Insets: schematic views of the ion channel structural evolution with increasing RH, with hydrophilic channels colored blue.
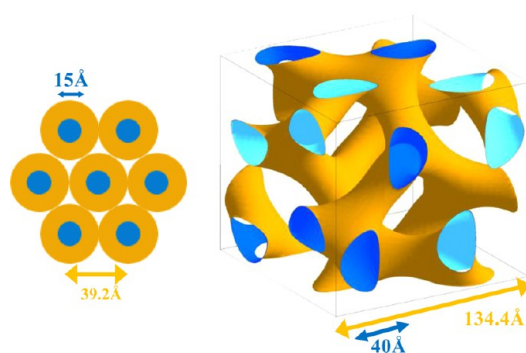

Figure 5. Models of Col$_{hd}$ and Cub$_{bi}$ gyroid phases drawn to scale. Ion conducting channels are shown in dark and light blue.

tion, in this case we estimate the average channel diameter to be 25.7 Å. However, we note that the channel diameter is not constant: the channels are thinnest in between the nodes whereas the junctions are much bulkier (see Figure 5). In the generated structure, all nodes are interconnected by channels, which means that at this water uptake the channels are not pinched off (as in the gyroid structure below the percolation threshold observed at 11.7%[33]). An analysis of the generated structure makes it possible to estimate the smallest and largest channel diameters of 25.0 and 40.8 Å, respectively. Clearly the cubic phases in these materials are superior for water and ion transport (see conductivity data in Figure S1), as these dimensions are much larger than the 15 Å hydrophilic channel in the columnar phase, and the cubic channel dimensions are close to those of established hydrated ion-conducting materials. Indeed, these channel dimensions strongly impact water diffusion, as we discuss below.

Sodium-23 NMR Measurements. As a quadrupolar nucleus with spin $I = 3/2$, ^{23}Na has been proven to be a powerful probe of the local environment around the nucleus in various materials,[34−38] as the line width and chemical shift of ^{23}Na NMR spectra are generally determined by the interaction between the electric quadrupole moment (a property of the nucleus) and electric field gradients (a property of the ~1 nm

scale surroundings).[39] This quadrupolar interaction is very sensitive to atomic bonds of the nucleus, the structure and composition of nearby molecules, and the symmetry of the surrounding charges.[39] Therefore, the study of quadrupolar nuclei with solid-state NMR can provide a wealth of information about the molecular-scale structure and dynamics.

Parts a−d of Figure 6 show the single pulse static ^{23}Na spectra of **A-Na** prepared at varying RH. Overall, the peak line width decreases as RH increases. At higher RH, sodium ions become on average more hydrated and the distance between sodium ions increases, reducing the asymmetry in the surrounding electronic environment. This results in decreased electric field gradients (EFGs) at the ^{23}Na nuclei, leading to reduced quadrupolar broadening. In addition, increased motional averaging further reduces the observed EFG. The significant decrease in line width from RH 55% to RH 86% indicates a phase change between these two hydration levels, in close agreement with GISAXS observations.

Parts e−h of Figure 6 show the single pulse magic angle spinning (MAS) ^{23}Na spectra of the **A-Na** material with a spinning speed of 10 kHz. The quadrupolar interaction is partially averaged under MAS, resulting in a spectrum that is much better resolved than a static spectrum, allowing us to identify various nonequivalent sodium sites in the system. We observe two ^{23}Na resonances at all hydration levels: a sharp peak at higher chemical shift values (~7 ppm) and a much broader peak at lower chemical shift values (peak locations and widths specified in Figure 6e−h). The narrow line shape at 7 ppm with fwhm =170 Hz indicates that the quadrupolar coupling is relatively small. On the basis of published work by O'Connell et al.,[41−44] we can reasonably assume that the sharp peak is the result of an individual Na$^+$ interacting with an individual RSO$_3^-$ group attached to an isolated ion pair or in similar environments producing very small EFGs. Combined with our discussions below regarding ^{1}H and ^{2}H relaxation and diffusion measurements, we suggest that those individual ion pairs locate predominantly in amorphous regions, or more precisely within domain boundaries of the material. While LC domains consist of well-packed wedge molecules, domain boundaries are much less populated. On the other hand, the chemical shift of the center of the broad peak arises from both isotropic chemical shift σ_{iso} and second-order quadrupolar shift σ_{2QS}, because most other interactions including first-order quadrupolar, dipolar, and chemical shift anisotropy are removed under magic angle spinning. While σ_{iso} is independent of external magnetic field ω_0, σ_{2QS} is inversely proportional to ω_0: $\sigma_{2QS} \propto \omega_Q^2/\omega_0$. In order to confirm the contribution of σ_{2QS}, we also obtained ^{23}Na MAS spectra at 79.2 MHz (data not shown). The broad peak is wider and more upfield shifted at this lower frequency, indicating that the second-order quadrupolar interaction is a major contribution to the broad peak line shape. Therefore, we assign the broad peak to Na$^+$ ion aggregates inside the ionic channels formed in LC mesophases.

As hydration increases, both peaks in the ^{23}Na MAS spectra shift toward 0 ppm. In ^{23}Na NMR, a single peak at 0 ppm is characteristic of aqueous Na$^+$ ions, since EFGs approach zero as Na$^+$ ions become fully hydrated and reside in a symmetric tetrahedral environment.[45] Therefore, the shift of the hydrated ion peak from 7 ppm at RH 33% to 0.4 ppm at RH 100% shows that Na$^+$ associated with amorphous wedges becomes increasingly hydrated as RH increases, and that nearly all Na$^+$ ions of amorphous wedges are hydrated at RH 100%. As RH increases, the broad peak shifts downfield and narrows,
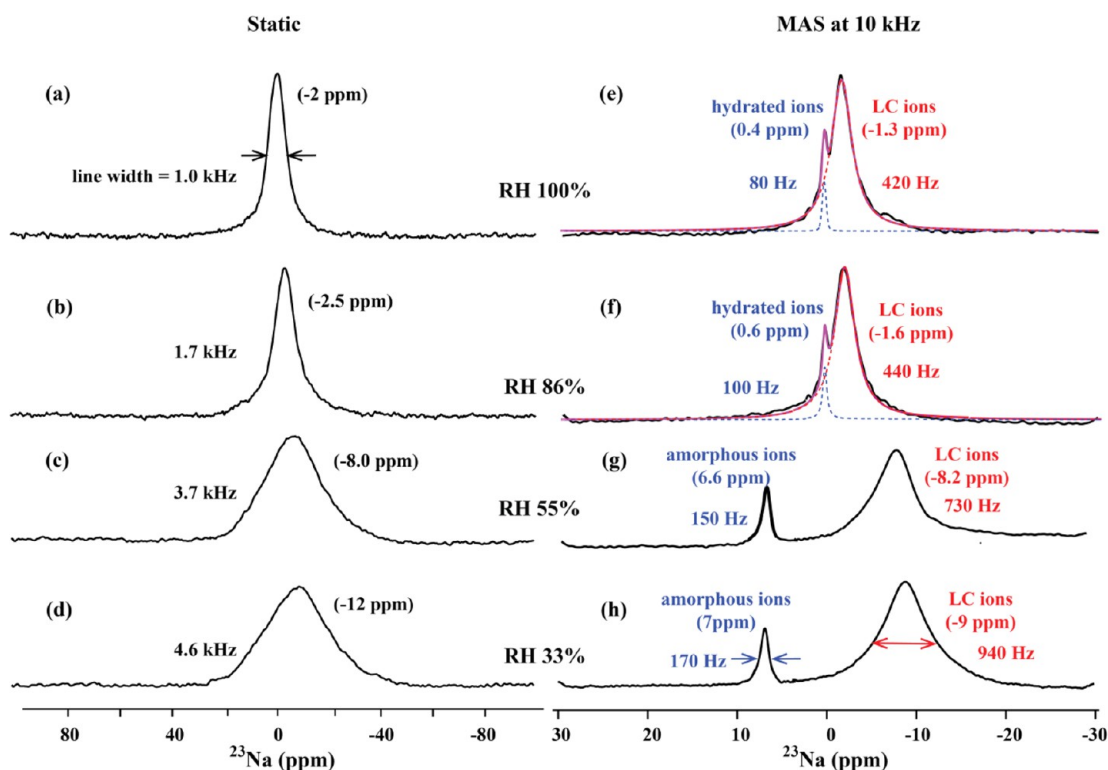
Figure 6. ^{23}Na solid-state static (left column, a-d) and MAS (right column, e-h) NMR spectra of **A-Na** salt at different RH. Note that different scales are used for the ppm axis of each column. A clear transition in Na quadrupolar interaction and mobility occurs between 55% and 86% RH, correlated with the phase transition observed by GISAXS. Two separate peaks are observed with MAS at 10 kHz. The sharp peak at 7 ppm at low RH is assigned to Na$^+$ of amorphous (domain boundary) wedges and contributes to $10 \pm 2\%$ of the total signal. The broad peak is assigned to Na$^+$ of wedges in the LC phases. By increasing RH, all Na$^+$ ions become completely or partially hydrated. We deconvolute the spectra in parts e and f to extract the fraction of each peak using matNMR,[40] and the hydrated sharp peak near 0 ppm is $8 \pm 1\%$ of the total signal.

suggesting a smaller second-order quadrupolar interaction and smaller EFGs as a result of increased hydration of Na$^+$ ions inside the ionic channels of LC domains. The increased molecular mobility at higher hydration also contributes to the reduction in line width. The broad peak at 100% RH appears at -1.3 ppm, which indicates that Na$^+$ ions inside the ionic channels do not become completely hydrated even under RH 100% with $\lambda(D_2O/SO_3^-) = 8.6$.

^{23}Na NMR can quantify the amount of wedge molecules present as amorphous wedges vs those within a mesophase. At 33% and 55% RH, the sharp peak contributes to $10 \pm 2\%$ of the total NMR signal. At 86% and 100% RH, the two peaks overlap, and deconvolution of the spectra is necessary to find the fraction of each peak. The deconvolution is shown as dotted lines in Figure 6, parts e and f, and we find that the hydrated Na peak at near 0 ppm contributes $8 \pm 1\%$ of the total signal for both 86% and 100% RH. We notice a slight decrease in the fraction of individual wedges at RH $\geq$ 86% compared to that of RH $\leq$ 55%, but the small decrease is within measurement error. In short, ^{23}Na MAS NMR spectra provide direct evidence of local structural disorder (the presence of 10% amorphous wedges). We discuss the molecular dynamics and translational motions of these amorphous wedges next.

^{1}H 1D NMR: Relaxation Measurements and Diffusion-Weighted Spectra. Figure 7 shows representative spectra of **A-Na** from several ^{1}H NMR experiments. ^{1}H MAS NMR data are shown at the top of Figure 7, static 1D NMR spectra are shown in blue for five humidity values, and diffusion-weighted spectra at the lowest gradient representative of 2D PGSTE

experiments are shown in red. We discuss each measurement below.

The ^{1}H MAS spectrum of **A-Na** at 18 kHz is shown in Figure 7 for the purpose of spectral assignment. In addition, Figure S2 displays ^{1}H MAS spectra of **A-Na** salt under all RH values with a spinning speed of 10 kHz. In agreement with the ^{23}Na measurements, all proton resonances become sharper and better resolved as RH increases, suggesting faster molecular motion at higher RH. With the help of a simple solution NMR spectrum (not shown), we assign the ^{1}H resonances as shown in Figure 7.

The blue lines of Figure 7 are the ^{1}HNMR static spectra of **A-Na** salt at different RH values. These spectra are broad and nearly featureless due to both inter- and intramolecular static dipolar interactions, which are not averaged on the NMR dipolar coupling time scale ($\sim$10 μs) due to significantly restricted motion. To gain information on the variety of molecular environments experienced by **A-Na** molecules in the sample, we collect T_2-weighted spectra (Figure S3) and measure T_2 decay constants under several RH conditions. For vacuum-dried **A-Na**, about 97% of the proton signal decays rapidly and nonexponentially with $T_2 < 2$ ms, due to the rigidity of the **A-Na** molecules in the Col$_{hd}$ phase, while the remaining resonance centered at 1.3 ppm decays with a single long $T_2 = 45$ ms. We conduct further dynamic studies of spin−lattice relaxation time T_1 and spin−lattice relaxation time in the rotating frame $T_{1\rho}$ (detailed discussions in Supporting Information), and these results corroborate our assumption that the long T_2 component at 1.3 ppm is not from the LC structures but from a more mobile amorphous region. Most
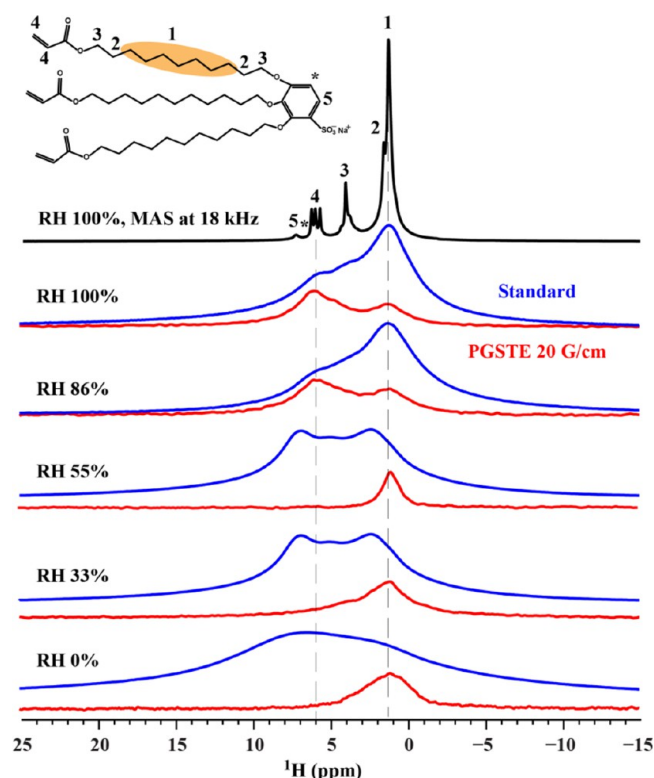
Figure 7. ^{1}H NMR spectra of **A-Na**. The ^{1}H MAS spectrum collected at 18 kHz and RH = 100% is at the top (black) for spectral assignment. The proton marked with an asterisk (∗) was not resolved. RH-dependent ^{1}H static 1D NMR spectra (top of each pair, blue) and the first (lowest gradient) spectra of a 2D PGSTE diffusion experiment (bottom of each pair, red) appear below. The 1D spectra (blue) show signal from all protons in the sample, while the diffusion-weighted spectra (red) show only proton signals with faster dynamics (longer T_2) that can be measured by PGSTE. At RH ≤ 55%, only amorphous wedge molecules move fast enough to probe diffusion. At RH ≥ 86%, wedges in LC phases are also accessible due to faster dynamics.

likely this amorphous component is the domain boundaries separating LC domains. This has dramatic implication for the PGSTE results of the RH ≤ 55% samples, as these diffusion experiments can only measure amorphous wedges, due to the T_2 weighting of these measurements. The T_2 values of all resonances increase with RH, indicating that all protons become increasingly mobile with water uptake. Considering the spectra at RH ≥ 86%, we notice a significant increase in proton signal intensity centered at 6.1 ppm when comparing these T_2-weighted spectra with τ = 5.6 ms (red lines of Figure S3) to the spectra with RH ≤ 55%. This shows that the mobility of protons in the hydrocarbon chains increases from the head to the tail of the chain in the LC structures. Therefore, we can observe both wedges in the LC domains (large amount, short T_2) and in the amorphous domain boundaries (small amount, long T_2) at RH ≥ 86%.

We also observe effects of T_2 weighting in the single diffusion-weighted spectra (in red) from the PGSTE diffusion measurements shown in Figure 7. In general, PFG-NMR diffusion experiments are conducted by recording successive NMR spectra as a function of gradient strength g, which allows for the display of a single NMR spectrum from the PGSTE experiment. This allows one to determine how much of the total signal available in the sample is probed by the diffusion measurement. Our diffusion measurements only show signals

from nuclei with relaxation times long enough to survive the gradient encoding times (2 × 5.2 ms =10.4 ms), when transverse relaxation (T_2) is active, and the 50 ms diffusion delay Δ, when longitudinal relaxation (T_1) is active. To visualize this, the red lines of Figure 7 show the first diffusion-weighted spectra (with the lowest g = 20 G/cm) of the 2D PGSTE experiments at different RH values. These traces closely mimic the T_2-weighted spectra with 5.6 ms spin echo delay in Figure S3.

As discussed in the previous paragraph, at RH ≤ 55%, protons from the columnar phase do not appear in the PGSTE diffusion experiments due to their short T_2 (<5 ms), and only the diffusion of amorphous wedges can be measured. At RH ≥ 86%, the dynamical situation changes drastically, and the chain-terminal acrylate protons (at 6.1 ppm) are now visible in the PGSTE measurements. As discussed above, we use the PGSTE peak at 6.1 ppm to measure the diffusion of the wedges pertinent to both the amorphous and liquid-crystalline regions.

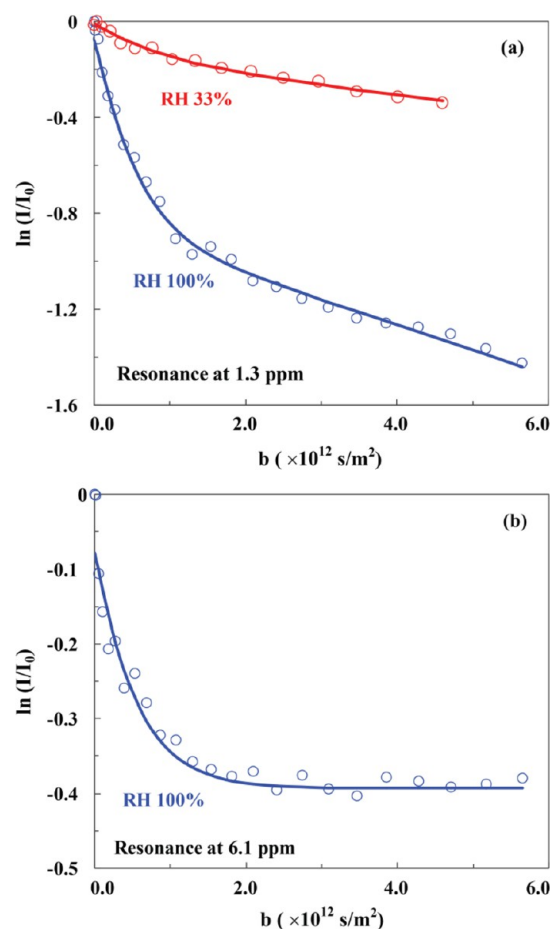**^{1}H Diffusion Measurements: Wedge Transport.** Figure 8 shows Stejskal−Tanner diffusion plots from the ^{1}H PGSTE

Figure 8. PGSTE diffusion experiments on **A-Na** equilibrated over D$_2$O. (a) Stejskal−Tanner plot of the ^{1}H resonance at 1.3 ppm from the methylene protons of **A-Na** molecules, showing fits to obtain two diffusion coefficients at both RH 33% and RH 100%. (b) Stejskal−Tanner plot of the ^{1}H resonance at 6.1 ppm from the chain-terminal acrylate protons of **A-Na** molecules at RH 100%, also fit to obtain two diffusion coefficients. The slow component (<1 × 10^{-15} m^2/s) is beyond our detection limit and is assigned to the slow diffusing wedges in the liquid crystal phase. In both plots the x-axis is the Stejskal−Tanner term of eq 1, $b = \gamma^2 g^2 \delta^2(\Delta - \delta/3)$.[23,24]
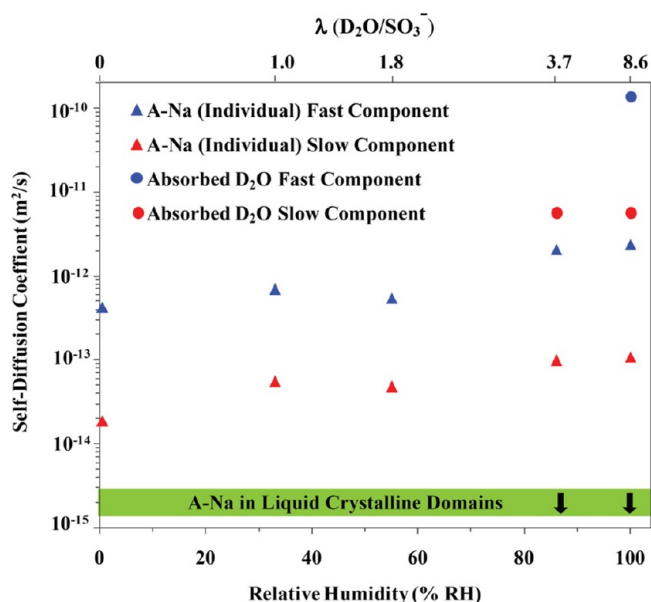
Figure 9. Diffusion coefficients of **A-Na** wedge molecules and absorbed D_2O vs RH and water uptake $\lambda(D_2O/SO_3^-)$. We assign the two diffusion components of the wedges to the individual wedges diffusing within and between LC domains, while the diffusion of the wedges in LC domains is very slow ($<10^{-15}$ m^2/s) and beyond our detection limit. The slow water diffusion component corresponds to wedges diffusing within amorphous domain boundaries, while the fast component is free water diffusing within the enlarged ionic channels of the bicontinuous phases.

measurements of **A-Na** salt equilibrated over D_2O. Figure 9 presents a summary of all the PGSTE results, including both the ^1H measurements on **A-Na** (this section) and the ^2H measurements on absorbed D_2O (next section). We conclude that wedges diffuse in two modes, with the fast component in the amorphous boundaries between LC domains and the slow component within the LC domains but existing as individual wedges not participating in LC packing.

At low RH, we observe clear two-component diffusion for the wedge molecules. For example, RH = 33% displays two-component diffusion with $D = 5 \times 10^{-14}$ m^2/s (88% amplitude) and 1.4×10^{-12} m^2/s (12%) for the resonance at 1.3 ppm. As discussed in the previous section, both diffusion coefficients correspond to the methylene protons of amorphous wedge molecules. The I_0 fitting parameter for these components represents the actual population percentage for the amorphous wedge molecules, since a single T_2 value is shared for the two components. The two-component diffusion presents more evidence of structural and dynamic heterogeneity in this supramolecular liquid crystal. We can calculate the diffusion length r using $\langle r^2 \rangle^{1/2} = (2D\Delta)^{1/2}$, which represents the statistical average distance a molecule has traveled during the diffusion time Δ.[46] Again using RH = 33% as an example, we find diffusion length of 70 nm for the slow component and 370 nm for the fast component with $\Delta = 50$ ms. Considering both the ^{23}Na SSNMR and ^1H diffusion data, we propose that the 10% of the material present as amorphous wedges exists in interfacial boundaries in between domains of the remaining 90% **A-Na** present in LC structures. We assign the fast component ($D = 1.4 \times 10^{-12}$ m^2/s) to the amorphous wedges diffusing within these domain boundaries, and the slow component ($D = 5 \times 10^{-14}$ m^2/s) to essentially individual wedges (wedge-counterion pairs) diffusing within columnar

domains but which do not participate in the columnar packing. Since NMR diffusion measurements reflect transport properties averaged over the entire sample, the existence of two clear diffusion components shows that the individual wedges are not exchanging between LC domains and domain boundaries of the material during the diffusion time of $\Delta = 50$ ms. In other words, wedge molecules are in fast exchange on all length scales smaller than 70 nm, requiring that the LC domains are ≥ 70 nm (the diffusion length of the slow component), and that the two different diffusion coefficients for the wedge molecules cannot be caused by differences in local molecular associations (<1 nm scale).[47]

At high RH (86% and 100%), the diffusion measurements become more complex. Similar to the low RH measurements, we find two diffusion components for the resonance at 1.3 ppm: $D = 1.0 \times 10^{-13}$ and 2.1×10^{-12} m^2/s (Figure 8a), however we cannot directly relate the I_0 fitting parameters to the percentage of each component due to multiple T_2 values. As above, we assign these D values to wedge molecules diffusing (1) within the mesophase and (2) in the amorphous regions that constitutes the domain boundary. In addition, we notice that the diffusion curve for the resonance at 6.1 ppm (Figure 8b) has a very slow and high intensity component that is beyond the detection limit of our PGSTE experiments ($D \leq 1 \times 10^{-15} m^2/s$). To investigate further, we perform another PGSTE measurement with long gradient encoding times ($\delta = 8$ ms), which only reports on the individual wedges with long T_2 components (data not shown). Here we obtain similar diffusion coefficients for both resonances at 1.3 and 6.1 ppm, which match the D values observed at 1.3 ppm with short encoding times ($\delta = 2$ ms). This shows that the peak at 6.1 ppm actually consists of three components: two components that are shared across both the 1.3 and 6.1 ppm peaks that are due to individual wedges in both the mesophase and domain boundaries, and one very slow component that is present only at 6.1 ppm. We assign this slowest diffusion coefficient $D \leq 1 \times 10^{-15}$ m^2/s to the slow diffusing wedges in the bicontinuous cubic or lamellar phases. While we are unable to measure the diffusion of the wedges in the columnar phase, it is a reasonable assumption that the Col_{hd} wedge molecules at low RH have even slower diffusion.

^2H Diffusion Measurements: Water Transport. In order to perfectly separate water diffusion measurements from wedge diffusion due to ^1H NMR spectral overlap from wedge-molecule peaks and to avoid deconvolution inaccuracies, we measure water (D_2O) diffusion by equilibrating samples over salt solutions in D_2O and performing ^2H NMR. We observe no detectable ^2H NMR signal at RH $\leq 55\%$ ($\lambda \leq 1.8$) due to this small amount of D_2O in the sample being strongly associated with ions in the columnar phase channels. Figure 10 shows ^2H 1D static spectra and PGSTE measurements of absorbed D_2O at RH 86% and 100%. Unlike ^2H spectra of absorbed D_2O in oriented liquid crystals or Nafion,[48] where the quadrupole splitting reveals the degree of LC alignment and order parameter of channel network matrix, here we only observe a broad singlet peak, indicating that no significant macroscopic orientational order of LC structures is present in these bulk samples. Furthermore, the broad peak results from the average signal from D_2O absorbed in both LC structures and amorphous regions. While the line width (fwhm) decreases only slightly from 260 to 210 Hz when increasing RH from 86% to 100%, the diffusion behavior is markedly different. The RH = 86% sample shows single component water diffusion (D
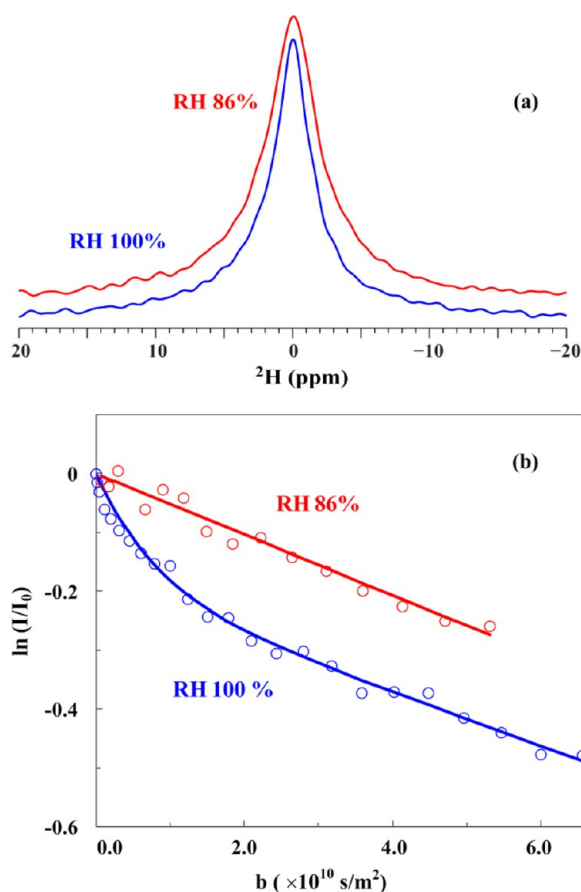
Figure 10. (a) ^{2}H static 1D NMR spectra of absorbed D_2O in the A-Na sample equilibrated over D_2O at RH 86% (top) and RH 100% (bottom). (b) Stejskal−Tanner plot of the ^{2}H peaks from the absorbed D_2O. We find a single diffusion coefficient ($D = 4.2 \times 10^{-12}$ m^2/s) at RH = 86%, and an additional faster component ($D = 1.7 \times 10^{-10}$ m^2/s) at RH = 100%.

= 4.2×10^{-12} m^2/s), but an additional faster component ($D = 1.7 \times 10^{-10}$ m^2/s) appears in the RH = 100% sample. The slow water component displayed by both the 86% and 100% RH samples has a diffusion coefficient very similar to the fast A-Na component, therefore it likely represents D_2O molecules diffusing within domain boundary regions with reasonably strong associations to the sulfonate group of individual A-Na molecules. In essence, the D_2O diffuses closely with a wedge-couterion pair. This assignment is supported by the ^{23}Na measurements, which show that Na$^+$ ions of individual wedges are nearly completely hydrated at RH ≥ 86%. The fast water component at RH = 100% is only an order of magnitude slower than the diffusion coefficient of pure D_2O,[49] suggesting that these D_2O molecules are relatively free to move within the enlarged ionic channels formed at the higher RH. This fast D_2O diffusion coefficient in A-Na is also nearly as fast as water diffusion in the benchmark conducting polymer membrane Nafion ($D = 3.5 \times 10^{-10}$ m^2/s) at similar hydration.[48] The fact that we only see the fast water motion in the bicontinuous cubic phase matches the hydrophilic channel dimensions from GISAXS, where the diameter of ionic channels increases from 15.0 Å in the columnar phase to between 25.0 and 40.8 Å in the cubic phase as the RH is increased from 55% (λ = 1.8) to 100% (λ = 8.6), as discussed above. Clearly, the cubic phases of A-Na are far superior for ion transport, especially at 100% RH.

■ CONCLUSION

We have presented a comprehensive picture of the rich structural and ion transport behaviors in supramolecular assemblies formed by amphiphilic wedge-shaped molecules (A-Na). The synergistic combination of GISAXS and multi-modal NMR provides detailed structural and transport properties of a supramolecular material to an extent rarely seen in the literature.

A-Na undergoes a transition from columnar to bicontinuous cubic phases with a simple increase in humidity. GISAXS, ^{23}Na solid-state NMR, and pulsed-field-gradient diffusion NMR all clearly show that the self-assembled A-Na material undergoes this change of LC phase, accompanied by drastic increases in ionic mobility at RH ≥ 86%. GISAXS measurements describe the hexagonal disordered columnar phase at lower RH and a mixture of gyroid, diamond and lamellar phases at higher RH. In addition, the lattice parameters and the estimated size of the hydrophilic ion channels for each phase increase with relative humidity; this change is small for the Col$_{hd}$ and lamellar phases and larger for bicontinuous cubic phases. The semimesomorphic nature of A-Na was quantified with ^{23}Na MAS NMR studies, showing the presence of a significant fraction (∼10%) of a disordered region at all RH values, which consists of amorphous domain boundary wedge molecules (with Na$^+$ counterions) that become nearly completely hydrated at RH ≥ 86%.

NMR diffusion studies on the amphiphiles (^{1}H) show that only amorphous wedges have relaxation times long enough to quantify with PGSTE measurements. We assign the slower PGSTE diffusion component (10^{-14} m^2/s) to individual wedges diffusing through LC phases and the faster component (10^{-12} m^2/s) to individual wedges diffusing within the amorphous boundaries between LC domains. The wedge molecules packed in LC phases are visible in PGSTE measurements only at high RH, but their very slow diffusion($<10^{-15}$ m^2/s) is beyond our diffusion detection limit. Overall, the domain boundaries of a mesomorphic material must be considered when investigating dynamic properties of the material itself or when measuring the transport of small molecules in the material. In some circumstances, the domain boundaries may be the dominant contributor to an observed property − a fact that has received little attention in the literature to date. Similar observations have been made in organic ionic plastic crystals, where domain boundary diffusion can dominate macroscopically measured transport.[50−53] The presence of domain boundaries may also disrupt the continuity of LC domains and thereby reduce water transport and ion conductivity.

NMR diffusion studies on adsorbed water (^{2}H$_2$O) show that D_2O molecules are tightly associated with the relatively narrow ionic channels (15.0 Å) in columnar phases at low RH. Two-component D_2O diffusion is observed at higher RH values. We assign the slow diffusion (10^{-12} m^2/s) to D_2O molecules diffusing within domain boundaries. The additional fast diffusion (10^{-10} m^2/s) obtained at high RH (λ = 8.6) is a result of relatively free water diffusing within the enlarged and interconnected ionic channels of the bicontinuous cubic phases.

Our combined NMR and GISAXS measurements show that the bicontinuous cubic phase is able to facilitate much faster ion transport than the columnar phase, as shown by the channel dimensions from GISAXS and the fast D_2O diffusion of the 100% RH sample. Water diffusion coefficients measured in the cubic phases at high hydration fall in the range of those

measured for benchmark ion conductors such as perfluorosulfonate ionomers at equivalent hydration.[48] These results show promise for controlled and informed design of next-generation ion conductors formed from tailored supramolecular building blocks.

■ ASSOCIATED CONTENT

Ⓢ Supporting Information

Ion conductivity and water uptakes $\lambda(H_2O/SO_3^-)$ of **A-Na** as a function of RH, estimation of the average channel size of supramolecular phases, ^1H solid-state MAS NMR spectra and peak assignments, ^1H static NMR relaxation (T_1, T_2, and $T_{1\rho}$) measurements and analysis. This material is available free of charge via the Internet at http://pubs.acs.org.

■ AUTHOR INFORMATION

Corresponding Authors

*E-mail: lmadsen@vt.edu.
*E-mail: Dimitri.Ivanov@uha.fr.

Author Contributions

‡These authors contributed equally to this work

Notes

The authors declare no competing financial interest.

■ ACKNOWLEDGMENTS

■ REFERENCES

(1) Lehn, J.-M. *Supramolecular Chemistry: Concepts and Perspectives*; Wiley-VCH Verlag GmbH & Co. KGaA: Weinheim, FRG, 1995.

(2) Nakanishi, T. *Supramolecular Soft Matter: Applications in Materials and Organic Electronics*; John Wiley & Sons, Inc.: Hoboken, NJ, 2012.

(3) Dong, B.; Sakurai, T.; Honsho, Y.; Seki, S.; Maeda, H. Cation Modules as Building Blocks Forming Supramolecular Assemblies with Planar Receptor−Anion Complexes. *J. Am. Chem. Soc.* **2013**, *135*, 1284−1287.

(4) Ye, X.; Chen, J.; Engel, M.; Millan, J. A.; Li, W.; Qi, L.; Xing, G.; Collins, J. E.; Kagan, C. R.; Li, J.; Glotzer, S. C.; Murray, C. B. Competition of Shape and Interaction Patchiness for Self-Assembling Nanoplates. *Nat Chem* **2013**, *5*, 466−473.

(5) Kato, T.; Mizoshita, N.; Kishimoto, K. Functional Liquid-Crystalline Assemblies: Self-Organized Soft Materials. *Angew. Chem., Int. Ed.* **2006**, *45*, 38−68.

(6) Yasuda, T.; Kato, T. Advanced Systems of Supramolecular Liquid Crystals. In *Supramolecular Soft Matter*; John Wiley & Sons, Inc.: New York, 2011; pp 281−299.

(7) Park, M. J.; Balsara, N. P. Anisotropic Proton Conduction in Aligned Block Copolymer Electrolyte Membranes at Equilibrium with Humid Air. *Macromolecules* **2010**, *43*, 292−298.

(8) Yuan, R.; Teran, A. A.; Gurevitch, I.; Mullin, S. A.; Wanakule, N. S.; Balsara, N. P. Ionic Conductivity of Low Molecular Weight Block Copolymer Electrolytes. *Macromolecules* **2013**, *46*, 914−921.

(9) O'Neill, M.; Kelly, S. M. Liquid Crystals for Charge Transport, Luminescence, and Photonics. *Adv. Mater.* **2003**, *15*, 1135−1146.

(10) Kishimoto, K.; Yoshio, M.; Mukai, T.; Yoshizawa, M.; Ohno, H.; Kato, T. Nanostructured Anisotropic Ion-Conductive Films. *J. Am. Chem. Soc.* **2003**, *125*, 3196−3197.

(11) Yoshio, M.; Mukai, T.; Ohno, H.; Kato, T. One-Dimensional Ion Transport in Self-Organized Columnar Ionic Liquids. *J. Am. Chem. Soc.* **2004**, *126*, 994−995.

(12) Shimura, H.; Yoshio, M.; Hoshino, K.; Mukai, T.; Ohno, H.; Kato, T. Noncovalent Approach to One-Dimensional Ion Conductors: Enhancement of Ionic Conductivities in Nanostructured Columnar Liquid Crystals. *J. Am. Chem. Soc.* **2008**, *130*, 1759−1765.

(13) Ichikawa, T.; Yoshio, M.; Hamasaki, A.; Kagimoto, J.; Ohno, H.; Kato, T. 3D Interconnected Ionic Nano-Channels Formed in Polymer Films: Self-Organization and Polymerization of Thermotropic Bicontinuous Cubic Liquid Crystals. *J. Am. Chem. Soc.* **2011**, *133*, 2163−2169.

(14) Yeh, M.-C.; Su, Y.-L.; Tzeng, M.-C.; Ong, C. W.; Kajitani, T.; Enozawa, H.; Takata, M.; Koizumi, Y.; Saeki, A.; Seki, S.; Fukushima, T. Amphiphilic Design of a Discotic Liquid-Crystalline Molecule for Dipole Manipulation: Hierarchical Columnar Assemblies with a 2D Superlattice Structure. *Angew. Chem., Int. Ed.* **2013**, *52*, 1031−1034.

(15) Zhang, H.; Li, L.; Möller, M.; Zhu, X.; Rueda, J. J. H.; Rosenthal, M.; Ivanov, D. A. From Channel-Forming Ionic Liquid Crystals Exhibiting Humidity-Induced Phase Transitions to Nanostructured Ion-Conducting Polymer Membranes. *Adv. Mater.* **2013**, *25*, 3543−3548.

(16) Rueda, D. R.; Nogales, A.; Hernández, J. J.; García-Gutiérrez, M.-C.; Ezquerra, T. A.; Roth, S. V.; Zolotukhin, M. G.; Serna, R. Stacking of Main Chain-Crown Ether Polymers in Thin Films. *Langmuir* **2007**, *23*, 12677−12681.

(17) Müller-Buschbaum, P. Grazing Incidence Small-Angle X-Ray Scattering: An Advanced Scattering Technique for the Investigation of Nanostructured Polymer Films. *Anal. Bioanal. Chem.* **2003**, *376*, 3−11.

(18) Lee, B.; Park, I.; Yoon, J.; Park, S.; Kim, J.; Kim, K.-W.; Chang, T.; Ree, M. Structural Analysis of Block Copolymer Thin Films with Grazing Incidence Small-Angle X-Ray Scattering. *Macromolecules* **2005**, *38*, 4311−4323.

(19) Young, J. F. Humidity Control in the Laboratory Using Salt Solutions—a Review. *J. Appl. Chem.* **1967**, *17*, 241−245.

(20) Fogden, A.; Hyde, S. T. Continuous Transformations of Cubic Minimal Surfaces. *Eur. Phys. J. B* **1999**, *7*, 91−104.

(21) Earl, W. L.; Vanderhart, D. L. Measurement of ^{13}C Chemical Shifts in Solids. *J. Magn. Reson.* **1982**, *48*, 35−54.

(22) Morcombe, C. R.; Zilm, K. W. Chemical Shift Referencing in Mas Solid State Nmr. *J. Magn. Reson.* **2003**, *162*, 479−486.

(23) Tanner, J. E. Use of the Stimulated Echo in Nmr Diffusion Studies. *J. Chem. Phys.* **1970**, *52*, 2523−2526.

(24) Stejskal, E. O.; Tanner, J. E. Spin Diffusion Measurements: Spin Echoes in the Presence of a Time-Dependent Field Gradient. *J. Chem. Phys.* **1965**, *42*, 288−292.

(25) Rancon, Y.; Charvolin, J. Epitaxial Relationships During Phase Transformations in a Lyotropic Liquid Crystal. *J. Phys. Chem.* **1988**, *92*, 2646−2651.

(26) Renaud, G.; Lazzari, R.; Leroy, F. Probing Surface and Interface Morphology with Grazing Incidence Small Angle X-Ray Scattering. *Surf. Sci. Rep.* **2009**, *64*, 255−381.

(27) Chvalun, S. N.; Shcherbina, M. A.; Bykova, V.; Blackwell, J.; Percec, V. Two- and Three-Dimensional Mesophases Formed by Monodendrons Based on Gallic Acid with Partially Fluorinated Alkyl Tails. *J. Polym. Sci. Ser. A* **2002**, *44*, 1281−1289.

(28) Squires, A. M.; Templer, R. H.; Seddon, J. M.; Woenkhaus, J.; Winter, R.; Narayanan, T.; Finet, S. Kinetics and Mechanism of the Interconversion of Inverse Bicontinuous Cubic Mesophases. *Phys. Rev. E* **2005**, *72*, 011502−011517.

(29) Seddon, J. M. Templer, R. H. *Polymorphism of Lipid-Water Systems. In Handbook of Biological Physics*; Elsevier Science B.V.: Amsterdam, 1995; Vol. *1*.

(30) Seddon, J. M.; Templer, R. H. Chapter 3 Polymorphism of Lipid-Water Systems. In *Handbook of Biological Physics*, Lipowsky, R.; Sackmann, E., Eds. North-Holland: Amsterdam, 1995; Vol. Vol. *1*, pp 97–160.

(31) Schwarz, U. S.; Gompper, G. Stability of Inverse Bicontinuous Cubic Phases in Lipid-Water Mixtures. *Phys. Rev. Lett.* **2000**, *85*, 1472–1475.

(32) Schwarz, U. S.; Gompper, G. Stability of Inverse Bicontinuous Cubic Phases in Lipid-Water Mixtures. *Phys. Rev. Lett.* **2000**, *85*, 1472–1475.

(33) Shearman, G. C.; Khoo, B. J.; Motherwell, M.-L.; Brakke, K. A.; Ces, O.; Conn, C. E.; Seddon, J. M.; Templer, R. H. Calculations of and Evidence for Chain Packing Stress in Inverse Lyotropic Bicontinuous Cubic Phases. *Langmuir* **2007**, *23*, 7276–7285.

(34) Orler, E. B.; Gummaraju, R. V.; Calhoun, B. H.; Moore, R. B. Effect of Preferential Plasticization on the Crystallization of Lightly Sulfonated Syndiotactic Polystyrene Ionomers. *Macromolecules* **1999**, *32*, 1180–1188.

(35) Kotecha, M.; Chaudhuri, S.; Grey, C. P.; Frydman, L. Dynamic Effects in MAS and MQMAS NMR Spectra of Half-Integer Quadrupolar Nuclei: Calculations and an Application to the Double Perovskite Cryolite. *J. Am. Chem. Soc.* **2005**, *127*, 16701–16712.

(36) Jia, Y.; Kleinhammes, A.; Wu, Y. NMR Study of Structure and Dynamics of Ionic Multiplets in Ethylene–Methacrylic Acid Ionomers. *Macromolecules* **2005**, *38*, 2781–2785.

(37) Yamamoto, Y.; Murakami, M.; Ikeda, R.; Deguchi, K.; Tansho, M.; Shimizu, T. The Local Structure around Sodium Ions in Poly(ethylene-*ran*-methacrylic acid) Ionomers Studied by ^{23}Na Solid-State NMR under a High Magnetic Field, 21.9 T. *Chem. Lett.* **2006**, *35*, 1058–1059.

(38) Lim, J. S.; Lee, Y.; Im, S. S. Influence of Ionic Association on the Nonisothermal Crystallization Kinetics of Sodium Sulfonate Poly-(Butylene Succinate) Ionomers. *J. Polym. Sci., Part B: Polym. Phys.* **2008**, *46*, 925–937.

(39) Jerschow, A. From Nuclear Structure to the Quadrupolar NMR Interaction and High-Resolution Spectroscopy. *Prog. Nucl. Magn. Reson. Spectrosc.* **2005**, *46*, 63–78.

(40) van Beek, J. D. Matnmr: A Flexible Toolbox for Processing, Analyzing and Visualizing Magnetic Resonance Data in Matlab. *J. Magn. Reson.* **2007**, *187*, 19–26.

(41) Oconnell, E. M.; Root, T. W.; Cooper, S. L. Morphological-Studies of Lightly-Sulfonated Polystyrene Using Na-23 NMR 0.1. Effects of Sample Composition. *Macromolecules* **1994**, *27*, 5803–5810.

(42) Oconnell, E. M.; Root, T. W.; Cooper, S. L. Morphological-Studies of Lightly Sulfonated Polystyrene Using Na-23 NMR 0.2. Effects of Solution Casting. *Macromolecules* **1995**, *28*, 3995–3999.

(43) Oconnell, E. M.; Root, T. W.; Cooper, S. L. Morphological-Studies of Lightly Sulfonated Polystyrene Using Na-23 NMR 0.3. Effects of Humidification and Annealing. *Macromolecules* **1995**, *28*, 4000–4006.

(44) OConnell, E. M.; Peiffer, D. G.; Root, T. W.; Cooper, S. L. Morphological Studies of Lightly Sulfonated Polystyrene Using Na-23 NMR: Effects of Polydispersity in Molecular Weight. *Macromolecules* **1996**, *29*, 2124–2130.

(45) Komoroski, R. A.; Mauritz, K. A. Na-23 Nuclear Magnetic-Resonance Study of Ionic Mobility and Contact Ion-Pairing in a Perfluorosulfonate Ionomer. *J. Am. Chem. Soc.* **1978**, *100*, 7487–7489.

(46) Callaghan, P. T., *Translational Dynamics & Magnetic Resonance: Principles of Pulsed Gradient Spin Echo NMR*; Oxford University Press Inc.: New York, 2011.

(47) Hou, J.; Li, J.; Mountz, D.; Hull, M.; Madsen, L. A. Correlating Morphology, Proton Conductivity, and Water Transport in Poly-electrolyte-Fluoropolymer Blend Membranes. *J. Membr. Sci.* **2013**, *448*, 292–299.

(48) Li, J.; Park, J. K.; Moore, R. B.; Madsen, L. A. Linear Coupling of Alignment with Transport in a Polymer Electrolyte Membrane. *Nat. Mater.* **2011**, *10*, 507–511.

(49) Holz, M.; Weingartner, H. Calibration in Accurate Spin-Echo Self-Diffusion Measurements Using ^{1}H and Less-Common Nuclei. *J. Magn. Reson.* **1991**, *92*, 115–125.

(50) Shekibi, Y.; Pas, S. J.; Rocher, N. M.; Clare, B. R.; Hill, A. J.; MacFarlane, D. R.; Forsyth, M. Surprising Effect of Nanoparticle Inclusion on Ion Conductivity in a Lithium Doped Organic Ionic Plastic Crystal. *J. Mater. Chem.* **2009**, *19*, 1635–1642.

(51) Jin, L.; Nairn, K. M.; Forsyth, C. M.; Seeber, A. J.; MacFarlane, D. R.; Howlett, P. C.; Forsyth, M.; Pringle, J. M. Structure and Transport Properties of a Plastic Crystal Ion Conductor: Diethyl-(methyl)(isobutyl)phosphonium Hexafluorophosphate. *J. Am. Chem. Soc.* **2012**, *134*, 9688–9697.

(52) Pringle, J. M.; Howlett, P. C.; MacFarlane, D. R.; Forsyth, M. Organic Ionic Plastic Crystals: Recent Advances. *J. Mater. Chem.* **2010**, *20*, 2056–2062.

(53) Kidd, B. E.; Lingwood, M. D.; Lee, M.; Gibson, H. W.; Madsen, L. A. Cation and Anion Transport in a Dicationic Imidazolium-Based Plastic Crystal Ion Conductor. *J. Phys. Chem. B* **2014**, DOI: dx.doi.org/10.1021/jp4084629.